Proton exchange membrane fuel cell contamination model: Competitive adsorption followed by a surface segregated electrochemical reaction leading to an irreversibly adsorbed product

Jean St-Pierre*

Department of Chemical Engineering, University of South Carolina, Swearingen Engineering Center, 301 Main Street, Columbia, SC 29208, USA

ABSTRACT

A generic, transient fuel cell kinetic loss mathematical model was developed for the case of contaminants that partially cover the catalyst surface with irreversibly adsorbed products. The model was derived using step changes in contaminant concentration, constant operating conditions and disregarding liquid water scavenging effects. The closed form solutions were validated using H_2S, SO_2 and COS data from a single source. The model needs to be validated against other data sets and transient operating conditions more representative of automotive applications. A method is proposed to determine kinetic rate constants and relies on tests with a reactant, a contaminant and, a reactant and a contaminant mixture. The method is useful to evaluate the presence of interactions between reactant and contaminant related adsorbates, and, to minimize electrode potential variations during controlled cell voltage measurements. Model parameters were similar for all contaminants suggesting a common adsorbate configuration. The model also expands the number of previously derived cases. All models in this inventory, derived with the assumption that the reactant is absent, lead to different dimensionless current vs. time behaviors similar to a fingerprint. These model characteristics facilitate contaminant mechanism identification. Model predictions include a limit of 0.7 ppb contaminant concentration in the reactant stream to minimize cell performance losses during the 5000 h automotive application life. This tolerance limit represents a worse case scenario because it does not take into account performance recovery resulting from drive cycle operation or the addition of mitigation strategies. A cell performance loss increase of 40% is also predicted for a catalyst loading decrease from 0.4 to 0.1 mg Pt cm^{-2}.

© 2010 Elsevier B.V. All rights reserved.

1. Introduction

Proton exchange membrane fuel cells (PEMFCs), an alternative power source for stationary, automotive and portable applications [1,2], are subjected to multiple sources of contaminants ranging from the ambient atmosphere, system/stack components, fuel and degradation products [3,4]. The number of known possible contaminants is large even before consideration of several potential sources of contamination that have not yet been investigated [3]. Furthermore, fuel cell system materials are still under development and are likely to be replaced in the future [5,6]. Thus, widely applicable generic mechanistic models with explicit analytical solutions are preferable to extract rate constants, set contaminant tolerance limits (predictions) and facilitate mechanism identification (contaminant classification) [3]. However, a complete set of such

models does not currently exist for all identified mechanisms. More specifically, a kinetic loss model for the case of partial performance recovery after contaminant exposure is needed.

Few relevant contamination models were published. An H_2S model was proposed but its derivation is based on a constant current assumption which complicates its application partly due to the rate constant dependence on potential [7]. Furthermore, the cell performance behavior after contamination was interrupted was not derived. A more general model version applicable to SO_x was also derived but it has the same limitations [8]. Subsequently, a different H_2S model was derived and its formulation allowed computations for the constant potential case [9]. However, the model derivation did not extend to the case of cell performance recovery after a contamination period and validation was not addressed. For either model cases, the derivation did not lead to explicit analytical solutions.

A generic model with explicit analytical solutions is derived for the case of partial cell performance recovery. The model is applicable to sulfur based gaseous contaminants such as SO_2, H_2S and COS that create sulfur based adsorbates under specific operating

* Tel.: +1 803 777 2581; fax: +1 803 777 8142.
  E-mail address: jeanst@cec.sc.edu.

Nomenclature

c_R	reactant volume fraction in the dry stream
c_X	contaminant volume fraction in the dry reactant stream
D	diffusion coefficient ($m^2\,s^{-1}$)
E_{anode}	anode potential (V)
$E_{cathode}$	cathode potential (V)
EPSA	Pt surface area to geometric active electrode area ratio ($m^2\,m^{-2}$)
Est_m	experimental estimates for specific model equations terms (m is an integer with a value of 1–8)
F	Faraday constant ($96,500\,C\,mol^{-1}$)
i	current density ($A\,m^{-2}$)
$i_{c_X=0}$	steady state current density in absence of a contaminant ($A\,m^{-2}$)
i_{R,ρ_1}	current density associated with a reactant and the catalyst area reversibly contaminated ($A\,m^{-2}$)
i_{R,ρ_2}	current density associated with a reactant and the catalyst area irreversibly contaminated ($A\,m^{-2}$)
i_{X,ρ_2}	current density associated with a contaminant and the catalyst area irreversibly contaminated ($A\,m^{-2}$)
i_{ρ_1}	current density associated with the catalyst area reversibly contaminated ($A\,m^{-2}$)
i_{ρ_2}	current density associated with the catalyst area irreversibly contaminated ($A\,m^{-2}$)
k'	lumped parameter defined by Eqs. (7) and (27)
k''	lumped parameter defined by Eqs. (8) and (28)
k_R	reaction rate constant associated with a reactant ($mol\,m^{-2}\,s^{-1}$)
$k_{R,ads}$	reactant adsorption rate constant ($mol\,s^{-1}\,N^{-1}$)
$k_{R,des}$	reactant desorption rate constant ($mol\,m^{-2}\,s^{-1}$)
k_X	forward reaction rate constant associated with a contaminant ($mol\,m^{-2}\,s^{-1}$)
$k_{X,ads}$	contaminant adsorption rate constant ($mol\,s^{-1}\,N^{-1}$)
$k_{X,des}$	contaminant desorption rate constant ($mol\,m^{-2}\,s^{-1}$)
k_{-X}	backward reaction rate constant associated with a contaminant ($mol\,m^{-2}\,s^{-1}$)
L	gas diffusion layer or ionomer layer thickness (m)
n	number of electrons exchanged in an electrochemical reaction
N_A	Avogadro's number ($6.02 \times 10^{23}\,mol^{-1}$)
p	reactant stream pressure ($N\,m^{-2}$)
p_s	water vapor saturation pressure ($N\,m^{-2}$)
R	cell resistance ($\Omega\,m^2$)
S_{Pt}	Pt site surface area ($0.76 \times 10^{-19}\,m^2$)
t	time (s)
V	cell voltage (V)
ε	void volume fraction
θ_{P_2}	reacted contaminant catalyst surface coverage
θ_R	reactant catalyst surface coverage
$\theta_{R,c_X=0}$	initial reactant catalyst surface coverage
θ_X	contaminant catalyst surface coverage
$\theta_{X,0}$	initial contaminant catalyst surface coverage
ρ	Pt site molar density ($mol\,m^{-2}$)
ρ_1	Pt site molar density associated with the reversibly adsorbed contaminant ($mol\,m^{-2}$)
ρ_2	Pt site molar density associated with the irreversibly adsorbed contaminant ($mol\,m^{-2}$)

conditions that do not desorb from the catalyst surface. The model is an extension of a prior model derived for a contaminant that leads to a complete performance recovery (complete desorption of contaminant adsorbate or reaction product) [10,11].

2. Model assumptions

Model assumptions were previously discussed and thus are mostly outlined here [10,11]. A new assumption which is relevant to the present model is discussed in more detail (presence of 2 contaminant adsorbates behaving differently).

Oxygen reduction is kinetically controlled under normal circumstances and involves a catalyst surface adsorbate R that produces a rapidly desorbing product P_1 (Fig. 1). This assumption is sufficient to cover automotive application cases because the mass transport regime is avoided by maintaining the cell voltage above 0.65–0.7 V to meet voltage efficiency and power converter input range constraints [12]. The overall reaction rate for the main reaction is larger than for the contamination reaction (pseudo-steady state) partly owing to the several orders of magnitude larger reactant concentrations. For instance, the oxygen adsorption/desorption time scale is estimated using the time scale associated with an oxygen concentration step change during fuel cell operation (air to pure oxygen and vice versa used for diagnostic purposes rather than for an application specific operation mode) which is of the order of a few minutes. This represents a worse case scenario considering the existence of parallel processes such as heat transfer relaxation. The estimated oxygen adsorption/desorption time scale is much smaller than the contamination time scale usually of the order of hours or more. The impact of reactant concentration changes along the flow field length which arise from consumption and gas crossover through the membrane is assumed to be minimal. This assumption is consistent with a relatively uniform current distribution during fuel cell operation as previously observed during NO$_2$
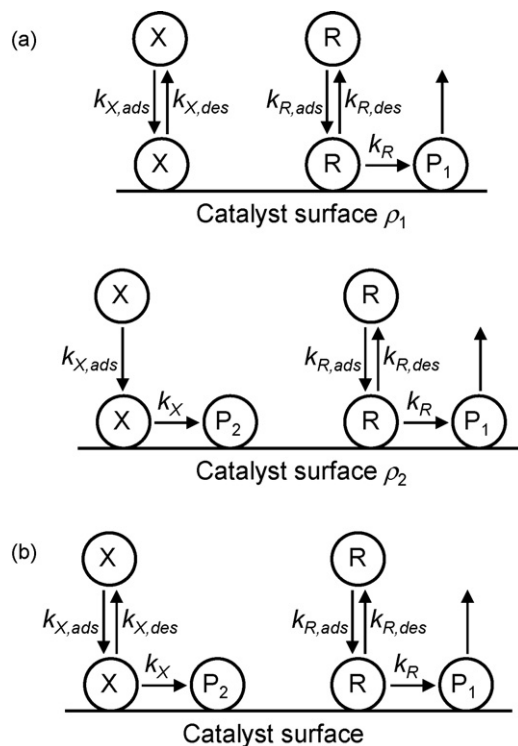

Fig. 1. Catalyst surface reactions for the case of (a) segregated sites and (b) uniform surface. X, R and P respectively represent the contaminant, the reactant and the product of an electrochemical reaction.

contamination [10]. On the catalyst surface, hydrogen oxidation is mechanistically similar to oxygen reduction (Fig. 1).

The contaminant transport from the fuel cell inlet to the catalyst is much more rapid than the contamination process time scale (hours or more). The time scale associated with gas transport in the flow-field channels is typically 0.06–0.6 s [13]. The H_2S, SO_2 and COS diffusion time scale (gas diffusion layer) is computed using $L^2/(D\varepsilon^{1.5})$, a thickness of 220 μm [14], a diffusion coefficient of 0.19–0.25 cm^2 s^{-1} [15], and a void volume fraction of 0.7 [14], leading to a range of 3.3–4.3 ms. The H_2S, SO_2 and COS diffusion time scale (ionomer layer) is computed using L^2/D, a thickness of 10 μm (this value is overestimated considering it constitutes a significant fraction of the catalyst layer), and an H_2S diffusion coefficient of 1.3×10^{-7} cm^2 s^{-1} in Nafion at 65 °C [16], leading to a value of 7.7 s (other species or other temperatures were not considered because data were not found). Therefore, the contaminant concentration is assumed to be spatially uniform. The contaminant X subsequently either reversibly adsorbs on a portion of the catalyst (Fig. 1a, top) or immediately reacts on the catalyst surface remainder and leads to a product P_2 (Fig. 1a, bottom). This scheme reproduces the main experimental observation and is apparently proposed for the first time. The partial performance recovery after exposure to a contaminant suggests the presence of two different adsorbates on the catalyst surface (one adsorbate desorbs whereas the other does not). This feature is not reproduced by the simpler scheme illustrated in Fig. 1b (see Appendix A). During contamination, the surface reaction leading to the irreversibly adsorbed product P_2 ensures that at the steady state, the surface coverage of reversibly adsorbed X decreases to zero. If the surface reaction is reversible to ensure that the adsorbate X partly covers the surface, then all adsorbates completely desorb from the surface during the recovery period.

The electrode potential is assumed to be constant thus fixing the electrochemically related rate constants. The inlet gases are assumed to be saturated with water vapor to avoid membrane dehydration and changes in ohmic losses [17]. The pressure and temperature are assumed to be constant because these parameters vary only slightly along the flow field channel [18]. All assumptions are sufficient to take account of two of the three identified contaminant effects (faradaic efficiency, surface coverage) [3]. The presence of adsorbate interactions with reactants, the third identified effect, may be assessed with the proposed experimental scheme to extract rate constants as pointed out in Sections 4.2 and 4.3.

Several other aspects were not considered in the model owing to the absence of relevant experimental data. For instance, the contaminant concentration is affected by the scavenging effect of liquid water, adsorption/reaction on carbon within the cell [19,20] and the presence of sulfur on the catalyst carbon support [21]. Therefore, even if a fraction of these effects are reduced by treating the catalyst carbon support or carbon gas diffusion layer to remove the sulfur [22–24], the contaminant concentration at the catalyst surface represents an effective value which is smaller than the contaminant concentration in the inlet stream.

3. Model equations

The model is derived for three different cases with a sequence of two-step changes in reactant and/or contaminant concentration (from 0 to a fixed value and back to 0). The first concentration change defines the contamination process whereas the second concentration change defines the recovery process. These different cases allow an unequivocal experimental determination of all model parameters as well as providing a model consistency validation test. The catalyst surface site balance constitutes the first derivation step. Subsequently, the contaminant adsorbates coverage is related to a reduction in catalyst surface area impacting the reaction rate.

3.1. Contaminant step changes in the presence of a reactant

The Pt surface reactant and contaminant mass balances for both catalyst regions during the contamination process are (Fig. 1a):

$$\rho_1 \frac{d\theta_R}{dt} \approx 0 = k_{R,ads}(1 - \theta_X - \theta_R)c_R(p - p_s) - k_{R,des}\theta_R - k_R\theta_R \tag{1}$$

$$\rho_1 \frac{d\theta_X}{dt} = k_{X,ads}(1 - \theta_X - \theta_R)c_X(p - p_s) - k_{X,des}\theta_X \tag{2}$$

$$\rho_2 \frac{d\theta_R}{dt} \approx 0 = k_{R,ads}(1 - \theta_{P_2} - \theta_R)c_R(p - p_s) - k_{R,des}\theta_R - k_R\theta_R \tag{3}$$

$$\rho_2 \frac{d\theta_{P_2}}{dt} = k_{X,ads}(1 - \theta_{P_2} - \theta_R)c_X(p - p_s) \tag{4}$$

The Pt site molar density $\rho = \rho_1 + \rho_2$ is defined as $EPSA/N_A S_{Pt}$. Eq. (1) gives the reactant surface coverage on ρ_1:

$$\theta_R = \frac{k_{R,ads}(1 - \theta_X)c_R(p - p_s)}{k_{R,ads}c_R(p - p_s) + k_{R,des} + k_R} = \theta_{R,c_X=0}(1 - \theta_X) \tag{5}$$

Replacement of Eq. (5) in Eq. (2) leads after simplification to:

$$\frac{\rho_1}{k' - k''\theta_X} d\theta_X = dt \tag{6}$$

$$k' = k_{X,ads}c_X(p - p_s)(1 - \theta_{R,c_X=0}) \tag{7}$$

$$k'' = k_{X,ads}c_X(p - p_s)(1 - \theta_{R,c_X=0}) + k_{X,des} \tag{8}$$

The solution is:

$$\theta_X = \frac{k'}{k''}(1 - e^{-k''t/\rho_1}) \tag{9}$$

A similar derivation is used with Eqs. (3) and (4) for the product P_2 coverage on ρ_2:

$$\theta_{P_2} = 1 - e^{-k't/\rho_2} \tag{10}$$

The total current at the electrode is:

$$i = i_{\rho_1} + i_{\rho_2} = i_{X,\rho_2} + i_{R,\rho_1} + i_{R,\rho_2} \approx i_{R,\rho_1} + i_{R,\rho_2} \tag{11}$$

because the contaminant is much less concentrated than the reactant by a factor of ∼10^4 in most cases (a few ppm). Also, i_R is proportional to $k_R\theta_R\rho$. Therefore, Eqs. (9)–(11) lead to:

$$\begin{aligned}
\frac{i}{i_{c_X=0}} &= \frac{k_R\theta_{R,c_X=0}(1 - \theta_X)\rho_1 + k_R\theta_{R,c_X=0}(1 - \theta_{P_2})\rho_2}{k_R\theta_{R,c_X=0}\rho_1 + k_R\theta_{R,c_X=0}\rho_2} \\
&= \frac{\rho_1(1 - \theta_X) + \rho_2(1 - \theta_{P_2})}{\rho} \\
&= \frac{1}{\rho}\left[\rho_1\left(1 - \frac{k'}{k''}(1 - e^{-k''t/\rho_1})\right) + \rho_2 e^{-k't/\rho_2}\right]
\end{aligned} \tag{12}$$

Eq. (12) has the following limiting forms:

$$t = 0, \quad \frac{i}{i_{c_X=0}} = 1 \tag{13}$$

$$t \to 0, \quad \frac{i}{i_{c_X=0}} = 1 - \frac{2k't}{\rho} \tag{14}$$

$$t \to \infty, \quad \frac{i}{i_{c_X=0}} = \frac{\rho_1}{\rho}\left(1 - \frac{k'}{k''}\right) \tag{15}$$

For $c_X \to 0$, Eqs. (7), (8) and (12) also accurately predict that $i/i_{c_X=0} = 1$. The Pt surface contaminant mass balance for the ρ_1 catalyst region during the recovery process is (Fig. 1a):

$$\rho_1 \frac{d\theta_X}{dt} = -k_{X,des}\theta_X \tag{16}$$

The solution is:

$$\theta_X = \theta_{X,0} e^{-k_{X,des}t/\rho_1} \tag{17}$$

The corresponding normalized current density with the assumption that a steady state was reached before recovery (P_2 coverage is equal to 1 on ρ_2) is:

$$\frac{i}{i_{c_X=0}} = \frac{\rho_1(1-\theta_X)}{\rho} = \frac{\rho_1}{\rho}(1-\theta_{X,0}e^{-k_{X,des}t/\rho_1}) \tag{18}$$

Eq. (15) in combination with Eq. (18) evaluated at $t=0$, provides an estimate for $\theta_{X,0}$:

$$\theta_{X,0} = \frac{k'}{k''} \tag{19}$$

Eq. (18) has the following limiting forms:

$$t \to 0, \quad \frac{i}{i_{c_X=0}} = \frac{\rho_1}{\rho}\left(1-\frac{k'}{k''}\right) + \frac{k'k_{X,des}t}{\rho k''} \tag{20}$$

$$t \to \infty, \quad \frac{i}{i_{c_X=0}} = \frac{\rho_1}{\rho} \tag{21}$$

3.2. Contaminant step changes in the absence of a reactant

Eqs. (9) and (10) still apply during the contamination process but Eqs. (7) and (8) need to be modified by setting $\theta_{R,c_X=0}$ to 0 (Eq. (5)). The current cannot be normalized because it is equal to 0 prior to the introduction of the electroactive contaminant. Thus, the current density on a real active area basis is:

$$i = i_X = nFk_X\theta_X = nFk_{X,ads}(1-\theta_{P_2})c_X(p-p_s)$$
$$= nFk_{X,ads}c_X(p-p_s)e^{-k't/\rho_2} \tag{22}$$

Eq. (22) has the following limiting forms:

$$t = 0, \quad i = nFk_{X,ads}c_X(p-p_s) \tag{23}$$

$$t \to 0, \quad i = nFk_{X,ads}c_X(p-p_s)\left(1-\frac{k't}{\rho_2}\right) \tag{24}$$

$$t \to \infty, \quad i = 0 \tag{25}$$

The current is equal to zero during the recovery process because an electrochemical reaction does not take place.

3.3. Reactant step changes in the absence of a contaminant

This case was previously derived by keeping the time derivative in Eq. (1) [11]. Only the main elements are reported here. For the positive step change, the current density is:

$$i = i_R = nFk_R\theta_R = nFk_R\frac{k''}{k'}(e^{k't/\rho}-1) \tag{26}$$

$$k' = -k_{R,ads}c_R(p-p_s) - k_{R,des} - k_R \tag{27}$$

$$k'' = k_{R,ads}c_R(p-p_s) \tag{28}$$

Eq. (26) limiting forms are:

$$t = 0, \quad i = 0 \tag{29}$$

$$t \to 0, \quad i = nFk_R\frac{k''}{\rho}t \tag{30}$$

$$t \to \infty, \quad i = -nFk_R\frac{k''}{k'} \tag{31}$$

For the negative step change, the current density is:

$$i = -nFk_R\frac{k''}{k'}e^{((k'+k'')t)/\rho} \tag{32}$$

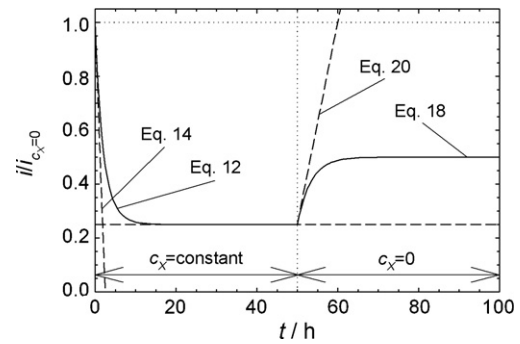**Fig. 2.** Effect of contamination (c_X = constant) and subsequent recovery (c_X = 0) on the cell normalized current density. ρ_1/ρ = 0.5, ρ_2/ρ = 0.5, k'/k'' = 0.5, k'/ρ = 0.2 h^{-1}, $k_{X,des}/\rho_1$ = 0.3 h^{-1}, k''/ρ_1 = 0.8 h^{-1}, and k'/ρ_2 = 0.4 h^{-1}.
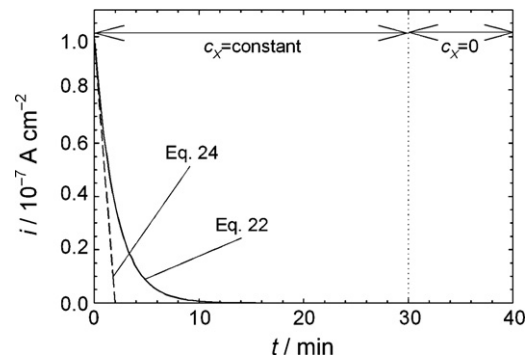

Fig. 3. Effect of contaminant step changes (from c_X = 0 to c_X = constant and vice versa) on the cell current density in absence of a reactant. $nFk_{X,ads}c_X(p-p_s)$ = 1 × 10^{-7} A cm^{-2} and k'/ρ_2 = 0.5 min^{-1}.
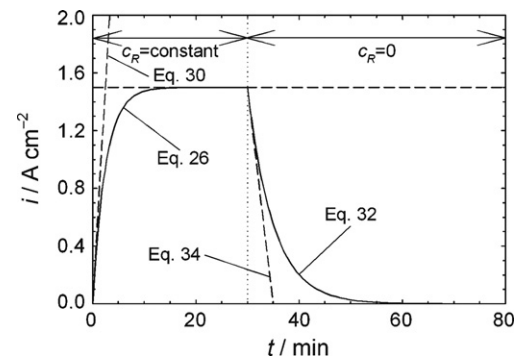

Fig. 4. Effect of reactant step changes (from c_R = 0 to c_R = constant and vice versa) on the cell current density in absence of contamination. nFk_Rk''/k' = −1.5 A cm^{-2}, k'/ρ = −0.4 min^{-1}, and $(k'+k'')/\rho$ = −0.2 min^{-1}.

whereas Eq. (32) limiting forms are:

$$t = 0, \quad i = -nFk_R\frac{k''}{k'} \tag{33}$$

$$t \to 0, \quad i = -nFk_R\frac{k''}{k'}\left(1+\frac{(k'+k'')t}{\rho}\right) \tag{34}$$

$$t \to \infty, \quad i = 0 \tag{35}$$

For the oxygen reduction reaction $n=4$ whereas for the hydrogen oxidation reaction $n=2$. Figs. 2–4 illustrate Eqs. (12), (18), (22), (26) and (32) for arbitrary rate constant values. Although 2 parallel processes take place during the contamination period (Eq. (12)), these are not distinguishable in Fig. 2. Linear approximations are highlighted in Fig. 2 for both initial contamination and recovery processes (Eqs. (14) and (20)). Most importantly, the steady state

Table 1
Summary of experimentally determined model parameters.

Parameter	Parameter value			Equation used for estimation
	H_2S	SO_2	COS	
ρ_1/ρ	0.3190	0.3480	0.3772	Curve fitting to Eq. (18)
ρ_2/ρ	0.6810	0.6520	0.6228	$\rho_2/\rho = 1 - \rho_1/\rho$
k'/k''	0.3082	0.3740	0.3072	Curve fitting to Eq. (18)
$k_{X,des}/\rho_1$ (h^{-1})	0.4410	0.3579	0.3343	Curve fitting to Eq. (18)
k'/ρ (h^{-1})	0.1895	0.2066	0.1880	Curve fitting to Eq. (12)
k''/ρ_1 (h^{-1})	1.9275	1.5874	1.6224	$k''/\rho_1 = (k'/\rho)(\rho/\rho_1)(k''/k')$
k'/ρ_2 (h^{-1})	0.2783	0.3169	0.3019	$k'/\rho_2 = (k'/\rho)(\rho/\rho_2)$

value for the recovery process does not reach the original value prior to the introduction of the contaminant ($i/i_{c_X=0} = 1$) but rather reaches a lower value (Eq. (21)). In Fig. 3, the total current associated with the contaminant reaction decreases to 0 (Eqs. (22) and (25)) as the catalyst surface ρ_2 is progressively and irreversibly covered by a contaminant product. The initial linear decay is also indicated (Eq. (24)). In Fig. 4 and in contrast with Fig. 3 transients, the current respectively increases from 0 (the reactant product desorbs and does not entirely block the catalyst surface, Eq. (26)) and decreases to 0 (Eq. (32)) after the reactant is introduced and its supply is interrupted. For each process, initial linear approximations are indicated (Eqs. (30) and (34)).

4. Results and discussion

4.1. Model validation

Few relevant fuel cell studies obtained with SO_2, H_2S, sulfides and mercaptans are available because most do not conform to the present model assumptions (constant electrode potential, successive positive and negative step changes in contaminant concentration, transients recorded until a steady state is reached) [25–39]. High temperature SO_2 and H_2S data obtained with polybenzimidazole based membrane/electrode assemblies do not show an irrecoverable loss [40]. Sensor studies are also irrelevant because operational parameters are set to ensure a reversible behavior (potential sufficient to oxidize SO_2 to SO_4^{2-}) [41]. Only one data set was found fulfilling model assumptions and is thus suitable for model validation [15].

Eq. (18) with 3 parameters (ρ_1/ρ, k'/k'', $k_{X,des}/\rho_1$) was first fitted to the recovery stage data. Subsequently, Eq. (12) with 4 parameters was simplified before fitting to the contamination stage data because 2 parameters were already determined (ρ_1/ρ, k'/k'') and the other 2 (k''/ρ_1, k'/ρ_2) were functions of an unknown parameter (k'/ρ) and other known (ρ_1/ρ, k'/k'') or easily derived (ρ_2/ρ) parameters (Table 1). Thus, the simplified Eq. (12) only had a single unknown parameter.

Fig. 5 illustrates the good agreement between the model and Gould et al. data for both contamination and recovery stages (all correlation coefficients are higher than 0.96) [15]. Transients were recorded just before a steady state was reached. Thus, additional data are needed to confirm model adequacy. Furthermore, the nature of the sulfur species does not appear to have an influence on the cell contamination kinetics as previously observed for SO_2 and H_2S [31]. Table 1 shows little parameter variability between all sulfur species. This observation may contain an important reaction mechanism clue and further illustrates the benefit of generic models. Presumably, a common adsorbed species may be produced from these three simple inorganic molecules (Section 4.3). This hypothesis is not expected to apply to larger more complex molecules such as aromatic thiophenes.
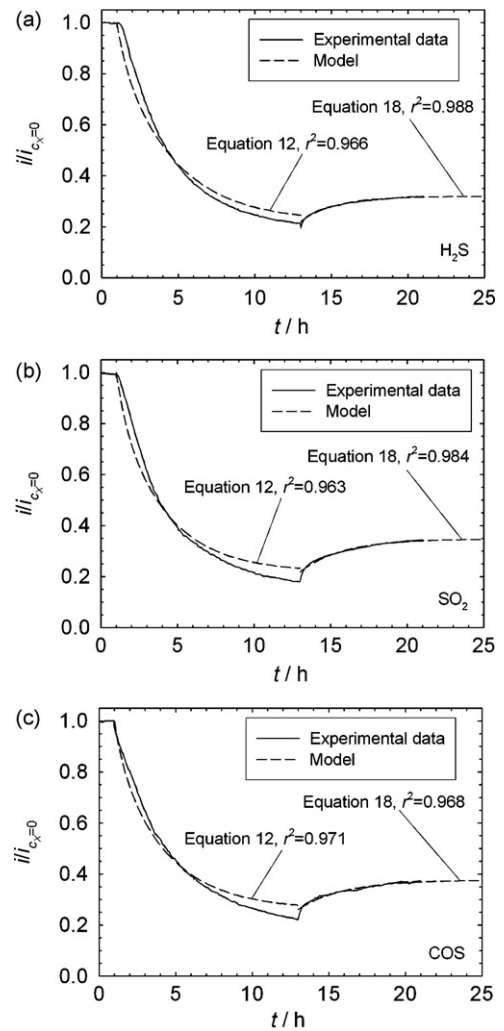

Fig. 5. Comparison between modeled and experimental contamination transients obtained with (a) H_2S, (b) SO_2 and (c) COS in air at a concentration of 1 ppm. Air/H_2, 0.5/0.25 l min^{-1}, 80 °C, 100% relative humidity, 0.6 V cell voltage.

4.2. Rate constants determination

Fig. 5 contamination data are insufficient to determine all 5 model rate constants. An experimental scheme is proposed to achieve such an objective (Fig. 6) and is based on the use of experimental data including fitted parameters and corresponding model relations at $t = 0$, the steady state or in the linear regime. It is assumed that all operating parameters such as temperature, pressure, total catalyst molar site density, etc. are either known or measured. The first element is the determination of reactant related rate constants as depicted in Fig. 6, step 1 (operation without contaminant and with step changes in c_R from a pre-determined value to 0 and vice versa). Eqs. (30) with (28) combined with the initial i slope (Est_1) lead to the following relation:

$$Est_1 = k_R k_{R,ads} \tag{36}$$

Eqs. (27), (28) and (32) and the $\ln(i)$ slope directly lead to the relation:

$$Est_2 = k_{R,des} + k_R \tag{37}$$

Eq. (31) with 27–28 and the steady state i value lead to the relation:

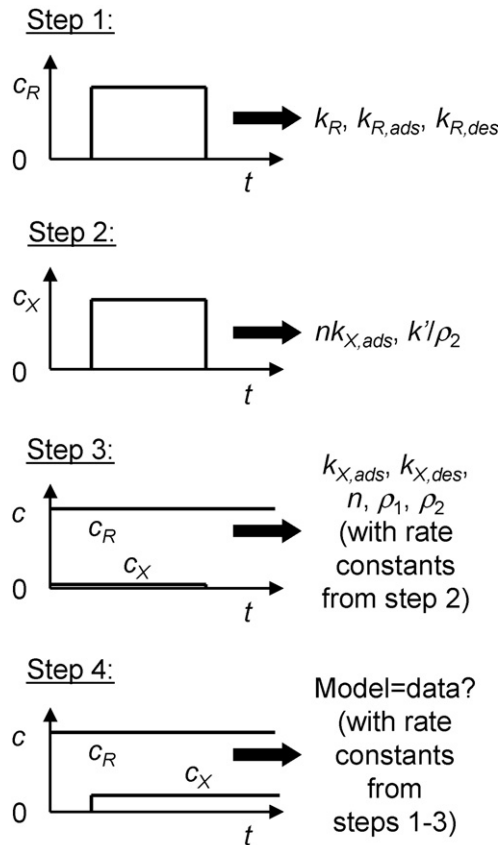$$Est_3 = \frac{-k_R k_{R,ads}}{k_{R,ads} c_R (p - p_s) + k_{R,des} + k_R} \tag{38}$$

Fig. 6. Experimental scheme to extract contamination model rate constants and to complete additional validation.

Fig. 7. Polarization curve for the cell used to obtain the contamination data reported in Fig. 5.

Use of Eqs. (36) and (37) to eliminate $k_{R,ads}$ and $k_{R,des}$ in Eq. (38) leads after simplification to:

$$k_R = \frac{-Est_1 c_R (p - p_s)}{Est_2 + (Est_1/Est_3)} \qquad (39)$$

Re-use of the k_R estimate from Eq. (39) into Eqs. (36) and (37) leads to $k_{R,ads}$ and $k_{R,des}$ estimates.

The second element of the experimental scheme is the determination of the contaminant rate constants (Fig. 6, step 2). Eqs. (23) and (24), the initial i value and slope give the following relations for $nk_{X,ads}$ and k'/ρ_2:

$$Est_4 = nk_{X,ads} \qquad (40)$$

$$Est_5 = nk_{X,ads} \frac{k'}{\rho_2} = Est_4 \frac{k'}{\rho_2} \qquad (41)$$

Eqs. (40) and (41) are insufficient to isolate the contaminant rate constants. The third element of the experimental scheme uses the recovery data in the presence of both contaminant and reactant to complete the contaminant rate constants determination (Fig. 6, step 3). Eqs. (20) and (21), the initial i value and slope and steady state i value yield ρ_1, k'/k'' and $k_{X,des}$ estimates:

$$Est_6 = \rho_1 \qquad (42)$$

$$Est_7 = \rho_1 \left(1 - \frac{k'}{k''}\right) = Est_6 \left(1 - \frac{k'}{k''}\right) \qquad (43)$$

$$Est_8 = \frac{k' k_{X,des}}{k''} = k_{X,des} \left(1 - \frac{Est_7}{Est_6}\right) \qquad (44)$$

Eq. (42) leads to ρ_2 from $\rho = \rho_1 + \rho_2$. Eq. (41) with the ρ_2 value leads to k' which in turn leads to $k_{X,ads}$ with Eq. (7) evaluated at $\theta_{R,c_X=0} = 0$. Finally, the $k_{X,ads}$ estimate leads to n by replacement in
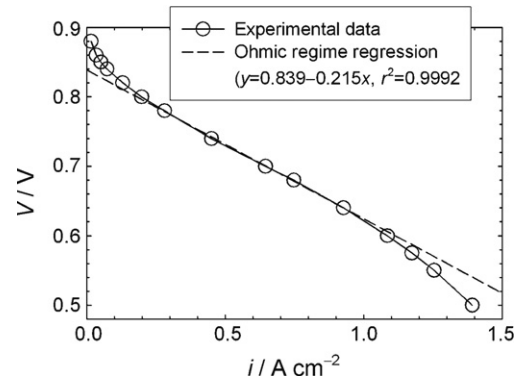
Eq. (40). The contaminant concentration used is low (Fig. 6, step 3) to minimize the presence of adsorbate interactions with reactants, an effect neglected in the model [3].

The last experimental scheme element is the computation of model curves for the case involving both reactant and contaminant during the contamination process (Fig. 6, step 4) using estimated rate constant values. Concordance between model predictions and experimental data will further validate the model for consistency. For instance, a significant discrepancy in the presence of a high contaminant concentration (Fig. 6, step 4 in comparison to Fig. 6, step 3) likely indicates the presence of adsorbate interactions with reactants.

4.3. Contamination mechanism

Fig. 5 validation data were obtained under a controlled cell voltage. The cathode potential is estimated based on the assumption that the hydrogen anode has a negligible overvoltage and on the cell resistance derived from the polarization curve ohmic regime (Fig. 7). The cathode potential is calculated from:

$$E_{cathode} = V + E_{anode} + iR \approx V + iR \qquad (45)$$

Eq. (45) respectively leads to $E_{cathode}$ = 0.836 and 0.643 V vs. H_2 electrode at the beginning ($i(0) \approx 1.1\,A\,cm^{-2}$) and end of the transient contamination ($i \approx 0.2\,A\,cm^{-2}$ at steady state). For the transient recovery, the cathode potential changes from 0.643 to 0.686 V vs. H_2 electrode ($i \approx 0.4\,A\,cm^{-2}$ at steady state). These values represent a maximum for two reasons. The polarization curve ohmic regime includes mass transfer contributions [42,43]. Therefore the polarization curve linear regime is pseudo-ohmic. Additionally, the ohmic resistance increases during the contamination process (Fig. 8). This behavior reflects an increase in ohmic resistance with a decrease in current density and is not affected by the presence of contaminants (presumably, a contaminant cation is not produced which would exchange with the membrane proton and increase cell resistance) [39]. As a result, the cathode potential change during contamination is significantly smaller (40–50 mV, Fig. 9) than estimated using the polarization curve pseudo-ohmic resistance ($\sim$190 mV). The change in cathode potential during the contamination/recovery processes is still significant and does not correspond to the constant electrode potential assumption used to derive the model. Model validation (Fig. 5) indicates that despite the significant change in electrode potential, good agreement was still found thus suggesting that the overall effect may not necessarily be large. Constant current operation is less desirable as potential changes of more than 0.4–0.5 V for H_2S [29,33–35] and 0.3 V for SO_2 [30] were observed. Preferably, a reference electrode should be considered but implementation is not necessarily trivial [44] especially if the additional requirement of contaminant insensitivity is added. The
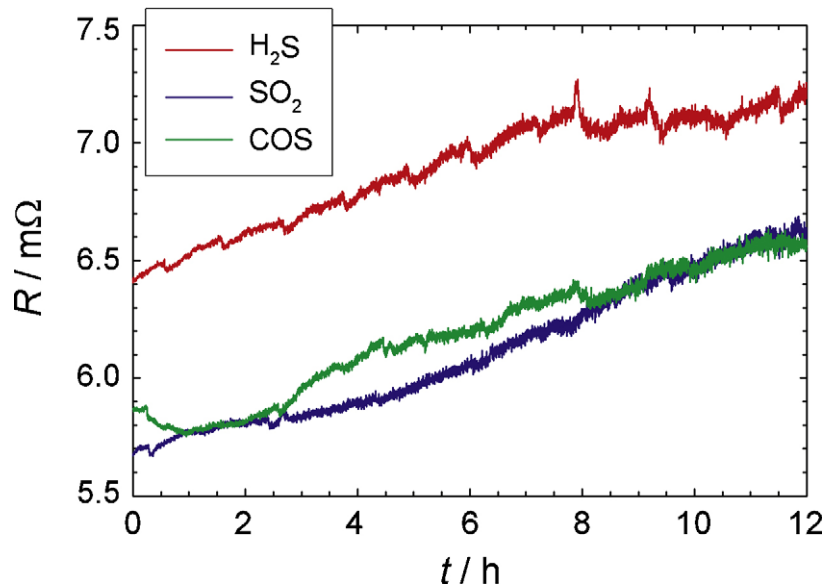
Fig. 8. Ohmic resistance evolution during contamination of the cell reported in Fig. 5.

ionomer is permeable to contaminants such as H_2S [16,45] and SO_2 [46]. Thus, contaminants can reach the reference electrode sensing surface and affect its potential. Other alternatives exist. It is possible to minimize electrode potential variations with the experimental scheme proposed to extract contamination rate constants (Fig. 6). For all experimental scheme steps, if the counter electrode is an H_2 electrode and the current is small (low contaminant and/or reactant concentration), then Eq. (45) indicates that the electrode potential of interest equals the cell potential. For the experimental scheme steps 3 and 4, a larger contaminant and/or reactant concentration could be used as long as the membrane is thin and the change in current is small to minimize the ohmic drop change contribution in Eq. (45). Cathode potential control ($V + iR$) [39] represents a feasible and more versatile option because operating conditions are less restrictive.

The state of adsorbed SO_2 on Pt was recently reviewed in the context of the hybrid sulfur cycle for hydrogen production [47]. This topic has not been fully resolved for several reasons includ-ing the significant number of sulfur oxidation states and absorbate structures, the dependence on electrode potential and analytical complexity (for example, infrared bands overlap, thereby obscuring adsorbate identification). Thus, adsorbate assignments are tentative and are provided to highlight commonalities between model assumptions and experimental data.

The presence of two distinct adsorbate species on the catalyst surface (Fig. 1a) is supported for the SO_2 in air case. Undissoci-ated SO_2 was detected on Pt in the potential range 0.65–1 V vs. RHE with adsorption taking place from both S and O atoms [48]. This species is ascribed to the reversibly adsorbed contaminant X (Fig. 1a). Other species could not be identified owing to equipment limitations. Recently, adsorbed sulfur species were shown to exist as S^0 at 0.05 V vs. RHE and as SO_4^{2-} (S^{6+}) at 1.4 V vs. RHE, with the oxidation state of the adsorbed sulfur species largely unknown (S^x), but ranging from elemental sulfur to sulfate ($x = 0$ to 6+), depending on electrode potential [49]. S^x species were stable within the potential range experienced during fuel cell operation
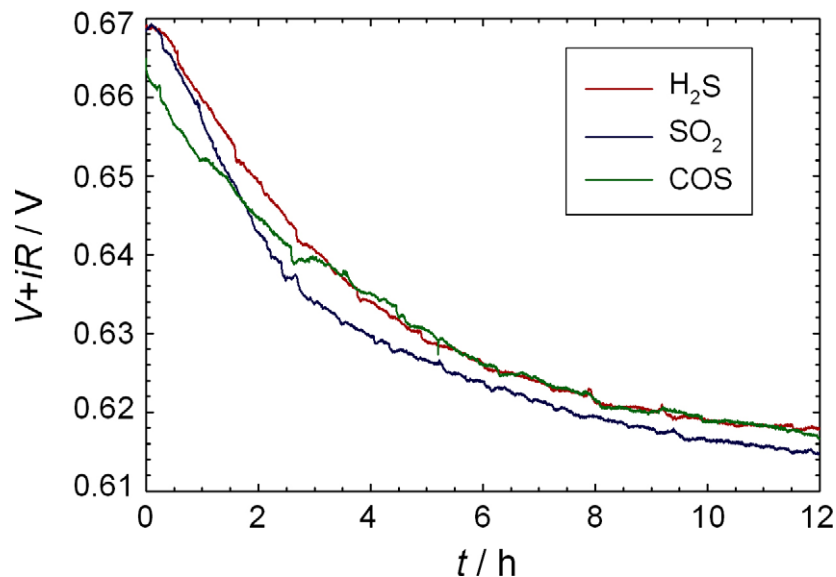

Fig. 9. Cathode potential evolution during contamination of the cell reported in Fig. 5.

(0.05–1 V vs. RHE) and are ascribed to the irreversibly adsorbed product P_2 (Fig. 1a). Adsorbed SO_2 was not detected on the catalyst surface. These results indicate that a possibility exists that both adsorbed SO_2 and irreversibly adsorbed S^x species are simultaneously present on the catalyst surface. Additional work is needed with fuel cell electrodes exposed to a gaseous stream rather than acidic solutions to verify this assumption. The existence of two distinct processes during fuel cell contamination with SO_2 has recently been ascertained although specific surface species were not identified [38]. For the other sulfur based contaminant species H_2S and COS, the similar cell performance dynamics (Fig. 5) suggests that the mechanism is similar to SO_2. Contaminant adsorption from the S atom is probable but other configurations are possible [48]. Therefore, additional tests are required to confirm the predominant adsorption from the S atom from all three tested contaminants (H_2S, SO_2, COS). This is especially important because conversion of H_2S and COS to SO_2 in the presence of O_2, and contaminant mass transfer limitations were also proposed to explain the similar fuel cell contamination behavior [15].

At steady state, the surface coverage by all contaminant species is computed using Eqs. (9) and (10). Experimentally determined average parameter values from Table 1 lead to:

$$\theta_X + \theta_{P_2} = \frac{\rho_1}{\rho}\frac{k'}{k''} + \frac{\rho_2}{\rho} = 0.11 + 0.65 \tag{46}$$

The measured surface coverage by cyclic voltammetry is equal to 0.44 at steady state [15]. Two reasons are provided to explain the discrepancy between the model derived value and the experimentally measured value. Because the cyclic voltammograms are completed after the contamination test, a fraction of the reversibly adsorbed contaminant X may have been lost reducing the experimental θ_X contribution. As for θ_{P_2}, the value determined by Eq. (46) represents an effective contribution. In other words, the real amount of contaminant adsorbates on the surface is less than computed from Eq. (46) because more than one Pt site is affected [50]. The measured surface coverage was correlated with an empirical exponential expression [15] similar in form to Eq. (9). This observation is consistent with the model because X adsorption is more rapid ($\rho_1/k'' = 0.58$ h average time scale, Table 1) than its conversion to a product P_2 ($\rho_2/k' = 3.34$ h average time scale, Table 1). Therefore, Eq. (9) represents the leading term for longer operation times (experimental data were initially collected after $\sim$3 h) [15]. Eq. (9) corrected by the ratio of P_2 sites ρ_2 to the total number of Pt sites ρ corresponds with the empirical expression. Finally, it is observed that the ratio of X sites ρ_1 to the total number of Pt sites ρ is equal to an average of 0.35 (Table 1). If it is assumed that the Pt catalyst particle size is equal to 2–4 nm [51], the fraction of edge and corner sites to the total number of sites is equal to 0.24–0.45 [52]. The correspondence between these 2 ratios is interesting but is too simplistic to reflect the actual situation. Recent X-ray absorption spectroscopy data [53] revealed that P_2 sites are not surface segregated. Rather, all catalyst sites are available to the product P_2 but their behavior is dependent on location. S^x species are more strongly bonded to edge and corner sites rather than plane sites. Therefore, more information is needed to identify the location of the X and P_2 sites.

The model was derived by assuming the absence of interactions between adsorbates (Langmuir kinetics) even if contradicting evidence exists [53]. Adsorbed SO_2 impacts the oxygen reduction mechanism by modifying product selectivity and favoring hydrogen peroxide rather than water as the concentration of the contaminant is increased [49]. Adsorbed sulfur also decreases the hydrogen oxidation reaction exchange current density [50]. The proposed experimental scheme to extract kinetic rate constants (Fig. 6) offers the possibility to evaluate the presence of adsorbate interactions with the reactant. Most of the information required to extract the kinetic rate constants involves a single species (steps 1 and 2 in Fig. 6) ruling out interactions between contaminant and reactant adsorbates. The procedure is completed by performing experiments with both reactant and contaminant (step 3 in Fig. 6). Adsorbate interactions are minimized by limiting the catalyst contaminant concentration and thus coverage [49]. Thus, kinetic rate constants are obtained with a minimum contribution from adsorbate interactions. Comparison between model predictions and experimental data obtained in the presence of both reactant and a high concentration of contaminant (step 4 in Fig. 6) will possibly indicate the presence of adsorbate interactions if significant discrepancies are observed.

Table 2 summarizes the features of the present model as well as other model versions derived for other cases using the same assumptions and method. For all cases, the total transient current i shows a similar behavior for all cases with the exception of the present case of an electroactive contaminant that leads to an irreversibly adsorbed product P_2. Thus, a distinction between all cases is not possible. By contrast, experiments performed without a reactant lead to the contaminant related current i_X and different transients for each case thus facilitating identification of the contamination mechanism with minimal testing requirements. The transient current i_R was validated using sensor data [11], but data are needed to validate the transient current i_X for the present model. Recent 1 ppm SO_2 in N_2 data [39] are difficult to interpret because the crossover H_2 (background current of 0.5–2 mA cm^{-2}) masks the SO_2 related current (3.6 μA cm^{-2} assuming a 6 electrons electrochemical reaction).

4.4. Model predictions

It is possible to predict the effect of contaminant concentration on key model parameters even if Fig. 5 experimental data were obtained for a single value of 1 ppm. The contaminant X adsorption time constant ρ_1/k'' (Eq. (9)) is linearly dependent on the contaminant concentration (Eq. (8)). Rearrangement of Eq. (8) in terms of estimated parameters (Table 1) and using Eq. (7) leads to:

$$\frac{k''}{\rho_1} = \frac{k' + k_{X,des}}{\rho_1} = \frac{k'}{\rho_2}\frac{\rho_2}{\rho}\frac{\rho}{\rho_1} + \frac{k_{X,des}}{\rho_1} \tag{47}$$

Three of the parameters in Eq. (47) are contaminant concentration independent (ρ_2/ρ, ρ_1/ρ, $k_{X,des}/\rho_1$) whereas the k'/ρ_2 term is linearly dependent on the contaminant concentration (Eq. (7)) and is directly scalable for other contaminant concentration values. The contaminant product P_2 reaction time constant ρ_2/k' (Eq. (10)) is thus also directly scalable for other contaminant concentration values. The contaminant X desorption time constant $\rho_1/k_{X,des}$ is independent of the contaminant concentration. All three time constants are illustrated in Fig. 10 as a function of the contaminant concentration. It is observed that the relative time constant values significantly vary with contaminant concentration. For a low contaminant concentration, ρ_2/k' dominates whereas for a large contaminant concentration, ρ_1/k'' is more important. Low contaminant concentrations are especially relevant to set fuel composition specifications which are also partly dependent on cell performance loss. The steady state $i/i_{c_X=0}$ value during the contamination process is given by Eq. (15) which is expressed as a function of estimated parameters (Table 1) using Eqs. (7) and (8):

$$\frac{\rho_1}{\rho}\left(1 - \frac{k'}{k''}\right) = \frac{\rho_1}{\rho}\left(1 - \frac{k'}{k' + k_{X,des}}\right) = \frac{\rho_1}{\rho}\left(1 - \frac{1}{1 + (k_{X,des}/\rho_1)(\rho_1/\rho)(\rho/\rho_2)(\rho_2/k')}\right) \tag{48}$$

Table 2
Summary of model behavior for different catalyst contamination kinetics.

Measured variable for step changes in c_X			$i\ (c_R \neq 0)$	$i_X\ (c_X = 0)$
Catalyst contamination kinetics	X electroactive ($k_X \neq 0$)	X reaction rds[a]	$=f(V)$	
		P_2 desorption rds[a]	$\neq f(V)$	
		Irreversible P_2 adsorption[b]	$\neq f(V)$	
	X electroinactive ($k_X = 0$)[a]		$\neq f(V)$	0

[a] Ref. [11].
[b] This work.

Three of the parameters in Eq. (48) are contaminant concentration independent (ρ_2/ρ, ρ_1/ρ, $k_{X,des}/\rho_1$) whereas the k'/ρ_2 term is linearly dependent on the contaminant concentration (Eq. (7)) and is directly scalable for other contaminant concentration values. The steady state $i/i_{c_X=0}$ value during the recovery process is given by Eq. (21) which is independent of the contaminant concentration (estimated parameter ρ_1/ρ in Table 1). Steady state $i/i_{c_X=0}$ values are illustrated in Fig. 10 as a function of the contaminant concentration. The cell performance loss is always at least equal to $1 - \rho_1/\rho$. For larger contaminant concentrations (>10 ppb), the cell performance loss is greater reaching 90% at ~2 ppm even if this additional part is recoverable ($\rho_1 k'/\rho k''$). The minimum performance loss is significant for all contaminant concentrations and is irrecoverable unless specific mitigation procedures are implemented. Additionally, the time constant ρ_2/k' appreciably increases for low contaminant concentrations and dominates contamination in this range. Thus, setting the contaminant concentration to less than ~0.7 ppb (ρ_2/k' curve, Fig. 10) ensures that the cell performance loss remains below $1 - \rho_1/\rho$ for the entire automotive application life (5000 h). This contaminant level is lower than the existing International Organization for Standardization specification of 4 ppb [54] and stretches existing analytical equipment

detection limits. However, the ~0.7 ppm tolerance limit represents a worse case scenario because it does not take into account performance recovery resulting from drive cycle operation (periods under open circuit or other potentials [15,47], etc.) or the addition of mitigation strategies (use of high electrode potentials [37], etc.).

Contamination and recovery model equations are dependent on both ρ_1/ρ and ρ_2/ρ parameters (Eqs. (12) and (18)) which represent the fraction of individual sites to the total number of catalyst sites. Thus, the contamination effect is dictated by the catalyst structure (types and relative proportions of sites) as well as its loading (a loading decrease leads to a larger cell performance loss). Fig. 5 data were obtained with a 0.4 mg Pt cm^{-2} cathode loading [15]. A reduction to 0.1 mg Pt cm^{-2} necessary to successfully commercialize fuel cells [5] increases the minimum contaminant concentration independent steady state loss $1 - \rho_1/\rho$ from 0.65 (Table 1) to 0.91. This represents a significant increase of 40%.

5. Conclusion

A PEMFC contamination model was derived for the case of an electroactive contaminant leading to an irreversibly adsorbed product. The model was purposefully derived to capture only essential processes to obtain analytical solutions and facilitate a widespread implementation (many different contaminants applicability). Model validation implies that the simplified approach has merit. A more complete model validation is desirable to obtain rate constants because only a limited amount of data was available. For implementation in automotive applications, the fuel cell response is expected to be a summation of responses obtained under constant operating conditions because the time scale associated with a change in operating conditions is much faster than the contamination time scale [3]. The model needs to be validated under such transient operating conditions. Other operating and cell design parameters effects of particular interest include electrode potential for both anode and cathode compartments, contaminant composition and concentration, temperature, and, catalyst composition [53] and loading. The identification of contaminant adsorbates and catalyst site types and relative abundance is also considered a valuable activity. Model predictions suggest the use of mitigation strategies and a revision of the proposed hydrogen composition specification.
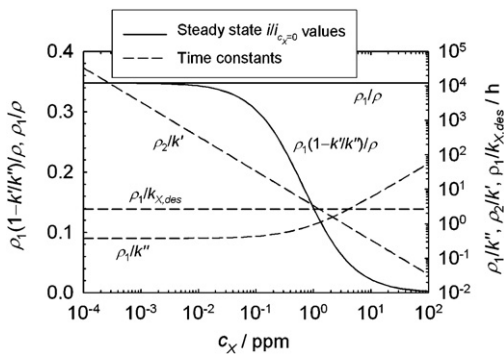

Fig. 10. Contamination processes steady state dimensionless current density changes and time constants as a function of contaminant concentration. Air + sulfur based gaseous contaminant/H$_2$, 0.5/0.25 l min^{-1}, 80 °C, 100% relative humidity, 0.6 V cell voltage. Curves were generated using average parameters from Table 1 ($\rho_1/\rho = 0.348$, $k_{X,des}/\rho_1 = 0.378$ h^{-1}, $k'/\rho_2 = 0.299$ h^{-1} for $c_X = 1$ ppm).

Acknowledgements

Appendix A.

The steady state catalyst surface site mass balances during the contamination process for the alternate mechanism depicted in Fig. 1b are:

$$0 = k_{R,ads}(1 - \theta_X - \theta_{P_2} - \theta_R)c_R(p - p_s) - k_{R,des}\theta_R - k_R\theta_R \quad (A.1)$$

$$0 = k_{X,ads}(1 - \theta_X - \theta_{P_2} - \theta_R)c_X(p - p_s) - k_{X,des}\theta_X - k_X\theta_X \quad (A.2)$$

$$0 = k_X\theta_X \quad (A.3)$$

Eq. (A.3) yields $\theta_X = 0$ and $\theta_{P_2} = 1 - \theta_R$ by simplifying Eq. (A.2). Replacement of θ_{P_2} by $1 - \theta_R$ in Eq. (A.1) leads to $\theta_R(k_{R,des} + k_R) = 0$, thus $\theta_R = 0$ and $\theta_{P_2} = 1$. The steady state catalyst surface site mass balances during the recovery process for the alternate mechanism depicted in Fig. 1b with the additional assumption that conversion of X to P_2 is reversible are:

$$0 = -k_{X,des}\theta_X - k_X\theta_X \quad (A.4)$$

$$0 = k_X\theta_X - k_{-X}\theta_{P_2} \quad (A.5)$$

Eq. (A.4) yields $\theta_X = 0$ and $\theta_{P_2} = 0$ by simplifying Eq. (A.5).

References

[1] W. Vielstich, H. Gasteiger, A. Lamm (Eds.), Handbook of Fuel Cells—Fundamentals, Technology and Applications, John Wiley and Sons, Chichester, West Sussex, England, 2003.
[2] J. Garche, C.K. Dyer, P. Moseley, Z. Ogumi, D. Rand, B. Scrosati (Eds.), Encyclopedia of Electrochemical Power Sources, Elsevier, Amsterdam, 2009.
[3] J. St-Pierre, in: F.N. Büchi, M. Inaba, T.J. Schmidt (Eds.), Polymer Electrolyte Fuel Cell Durability, Springer, New York, 2009, pp. 289–321.
[4] A. Kabasawa, J. Saito, K. Miyatake, H. Uchida, M. Watanabe, Electrochim. Acta 54 (2009) 2754–2760.
[5] H.A. Gasteiger, S.S. Kocha, B. Sompalli, F.T. Wagner, Appl. Catal. B 56 (2005) 9–35.
[6] M.A. Hickner, H. Ghassemi, Y.S. Kim, B.R. Einsla, J.E. McGrath, Chem. Rev. 104 (2004) 4587–4612.
[7] Z. Shi, D. Song, J. Zhang, Z.-S. Liu, S. Knights, R. Vohra, N. Jia, D. Harvey, J. Electrochem. Soc. 154 (2007) B609–B615.
[8] Z. Shi, D. Song, H. Li, K. Fatih, Y. Tang, J. Zhang, Z. Wang, S. Wu, Z.-S. Liu, H. Wang, J. Zhang, J. Power Sources 186 (2009) 435–445.
[9] A.A. Shah, F.C. Walsh, J. Power Sources 185 (2008) 287–301.
[10] J. St-Pierre, N. Jia, R. Rahmani, J. Electrochem. Soc. 155 (2008) B315–B320.
[11] J. St-Pierre, J. Electrochem. Soc. 156 (2009) B291–B300.
[12] J. Larminie, A. Dicks, Fuel Cell Systems Explained, second ed., Wiley, 2003, p. 333 (Figure 10.1).
[13] J. Diep, D. Kiel, J. St-Pierre, A. Wong, Chem. Eng. Sci. 62 (2007) 846–857.
[14] J. St-Pierre, A. Wong, J. Diep, D. Kiel, J. Power Sources 164 (2007) 196–202.
[15] B.D. Gould, O.A. Baturina, K.E. Swider-Lyons, J. Power Sources 188 (2009) 89–95.
[16] V.A. Sethuraman, S. Khan, J.S. Jur, A.T. Haug, J.W. Weidner, Electrochim. Acta 54 (2009) 6850–6860.
[17] J. St-Pierre, J. Electrochem. Soc. 154 (2007) B724–B731.
[18] D.P. Wilkinson, J. St-Pierre, J. Power Sources 113 (2003) 101–108.
[19] C. Quijada, J.L. Vázquez, Electrochim. Acta 50 (2005) 5449–5457.
[20] D. López, R. Buitrago, A. Sepúlveda-Escribano, F. Rodríguez-Reinoso, F. Mondragón, J. Phys. Chem. C 112 (2008) 15335–15340.
[21] K.E. Swider, D.R. Rolison, J. Electrochem. Soc. 143 (1996) 813–819.
[22] K.E. Swider, D.R. Rolison, Langmuir 15 (1999) 3302–3306.
[23] K.E. Swider, D.R. Rolison, Electrochem. Solid-State Lett. 3 (2000) 4–6.
[24] P.K. Dutta, R.A. Rozendal, Z. Yuan, K. Rabaey, J. Keller, Electrochem. Commun. 11 (2009) 1437–1440.
[25] R. Mohtadi, W.-K. Lee, J.W. Van Zee, Appl. Catal. B 56 (2005) 37–42.
[26] R. Mohtadi, W.-K. Lee, S. Cowan, J.W. Van Zee, M. Murthy, Electrochem. Solid-State Lett. 6 (2003) A272–A274.
[27] J.M. Moore, P.L. Adcock, J.B. Lakeman, G.O. Mepsted, J. Power Sources 85 (2000) 254–260.
[28] D. Imamura, M. Akai, S. Watanabe, J. Power Sources 152 (2005) 226–232.
[29] W. Shi, B. Yi, M. Hou, F. Jing, P. Ming, J. Power Sources 165 (2007) 814–818.
[30] F. Jing, M. Hou, W. Shi, J. Fu, H. Yu, P. Ming, B. Yi, J. Power Sources 166 (2007) 172–176.
[31] Y. Nagahara, S. Sugawara, K. Shinohara, J. Power Sources 182 (2008) 422–428.
[32] I.G. Urdampilleta, F.A. Uribe, T. Rockward, E.L. Brosha, B.S. Pivovar, F.H. Garzon, Electrochem. Soc. Trans. 11 (2007) 831–842.
[33] B.M. Besancon, V. Hasanov, R. Imbault-Lastapis, R. Benesch, M. Barrio, M.J. Mølnvik, Int. J. Hydrogen Energy 34 (2009) 2350–2360.
[34] W. Shi, B. Yi, M. Hou, Z. Shao, Int. J. Hydrogen Energy 32 (2007) 4412–4417.
[35] W. Shi, B. Yi, M. Hou, F. Jing, H. Yu, P. Ming, J. Power Sources 164 (2007) 272–277.
[36] J. Fu, M. Hou, C. Du, Z. Shao, B. Yi, J. Power Sources 187 (2009) 32–38.
[37] R. Mohtadi, W.-K. Lee, J.W. Van Zee, J. Power Sources 138 (2004) 216–225.
[38] Y. Zhai, G. Bender, S. Dorn, R. Rocheleau, J. Electrochem. Soc. 157 (2010) B20–B26.
[39] O.A. Baturina, K.E. Swider-Lyons, J. Electrochem. Soc. 156 (2009) B1423–B1430.
[40] Y. Garsany, B.D. Gould, O.A. Baturina, K.E. Swider-Lyons, Electrochem. Solid-State Lett. 12 (2009) B138–B140.
[41] G. Schiavon, G. Zotti, R. Toniolo, G. Bontempelli, Analyst 116 (1991) 797–801.
[42] J. St-Pierre, D.P. Wilkinson, S. Knights, M. Bos, J. New Mater. Electrochem. Syst. 3 (2000) 99–106.
[43] J. St-Pierre, N. Jia, J. New Mater. Electrochem. Syst. 5 (2002) 263–271.
[44] P. Piela, T.E. Springer, J. Davey, P. Zelenay, J. Phys. Chem. C 111 (2007) 6512–6523.
[45] E.L. Brosha, T. Rockward, F.A. Uribe, F.A. Garzon, J. Electrochem. Soc. 157 (2010) B180–B186.
[46] M.C. Elvington, H. Colón-Mercado, S. McCatty, S.G. Stone, D.T. Hobbs, J. Power Sources 195 (2010) 2823–2829.
[47] J.A. O'Brien, J.T. Hinkley, S.W. Donne, S.-E. Lindquist, Electrochim. Acta 55 (2010) 573–591.
[48] C. Quijada, A. Rodes, F. Huerta, J.L. Vázquez, Electrochim. Acta 44 (1998) 1091–1096.
[49] Y. Garsany, O.A. Baturina, K.E. Swider-Lyons, J. Electrochem. Soc. 154 (2007) B670–B675.
[50] J.J. Pietron, J. Electrochem. Soc. 156 (2009) B1322–B1328.
[51] P.J. Ferreira, G.J. la O', Y. Shao-Horn, D. Morgan, R. Makharia, S. Kocha, H.A. Gasteiger, J. Electrochem. Soc. 152 (2005) A2256–A2271.
[52] K. Kinoshita, J. Electrochem. Soc. 137 (1990) 845–848.
[53] D.E. Ramaker, D. Gatewood, A. Korovina, Y. Garsany, K.E. Swider-Lyons, J. Phys. Chem. C, in press.
[54] ISO/CD 14687-2:2009.